Heliyon 9 (2023) e20674

Contents lists available at ScienceDirect

Heliyon

journal homepage: www.cell.com/heliyon

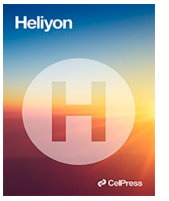

ZnO-based heterojunction catalysts for the photocatalytic degradation of methyl orange dye

Darlington C. Ashiegbu [a,*], Herman J. Potgieter [a,b]

[a] School of Chemical and Metallurgical Engineering, University of the Witwatersrand Johannesburg, Private Bag X3 PO Wits 2050, Johannesburg, South Africa
[b] Department of Natural Science, Manchester Metropolitan University, Chester Street, M1 5GD, Manchester, UK

ARTICLE INFO

Keywords:
Methyl orange
Photocatalysts
ZnO-Based heterojunction
Reaction kinetics
Waste treatment

ABSTRACT

In this study, a variety of ZnO-based heterojunctions with disparate wt.% doping of WO_3 and BiOI have been prepared for the photodestruction of methyl orange (MO) dye in aqueous solution. The composites were analysed by scanning electron microscopy, energy-dispersive X-ray spectroscopy, X-ray diffraction, optical studies, and nitrogen adsorption-desorption isotherms. The SEM images revealed non-uniform surfaces of the ZnO–BiOI based composites while mostly nodular morphology was observed for all three samples of ZnO-WO_3. As the WO_3 loading increased, more clustering was detected. The analysed samples exhibited characteristic peaks representative of the triclinic phase of WO_3 and the hexagonal wurtzite structure of ZnO, while the diffractogram observed from the materials displayed distinct peaks corresponding to the crystalline phases of both BiOI and ZnO in their pure forms. Further evidence of the samples' characteristics includes the presence of distinct crystalline patterns without any impurity peaks, a red shift in the absorption spectra of the heterostructure, the detection of only the reference elements, and mostly Type IV isotherm adsorption. This study identified the ZnO-[10%]BiOI and ZnO-[10%]WO_3 heterojunctions as the best performing photocatalysts, as MO was completely destroyed in 120 and 90 min, respectively. Thus, confirming 10% wt. as the optimal doping concentration for the best photo-activity in this study. The impact of varying process parameters demonstrates that at an elevated photocatalyst mass of 40 mg, both heterojunctions effectively degraded MO. The photodegradation efficiency of MO was more pronounced in strong acidic conditions (pH 2) when compared to high alkaline conditions (pH 11) for the ZnO-[10%]BiOI heterostructure. However, a decrease in performance was observed for both strong acidic and high alkaline pH values when the ZnO-[10%]WO_3 heterostructure was applied. The kinetic analysis of the photodegradation study reveals that all the photodegradation experiments can be represented by the pseudo-first-order kinetic model. The findings from this investigation propose that the ZnO-[10%]BiOI heterojunction photocatalyst holds significant potential for the effective treatment of dye-contaminated wastewater.

1. Introduction

The textile industry is an essential consumer-focused industry. However, this sector is one of the highest contributors to global

* Corresponding author.
E-mail address: darlington.ashiegbu@wits.ac.za (D.C. Ashiegbu).

https://doi.org/10.1016/j.heliyon.2023.e20674
Received 26 June 2023; Received in revised form 26 September 2023; Accepted 4 October 2023
Available online 5 October 2023

pollution in addition to its high consumption of fuels and chemicals [1]. Textile industries contribute significantly to water pollution worldwide through the discharge of wastewater containing dyes. Due to inefficiencies in the dye-making process, a considerable amount of dyes are lost. Approximately 2–20% of these lost dyes are directly released into various environmental components as aqueous effluents [2,3]. The wastewater originating from printing and dye industries is distinguished by a high concentration of complex pollutants, high levels of Biochemical Oxygen Demand (BOD) and Chemical Oxygen Demand (COD), and exhibits poor biodegradability [4]. In addition, the wastewater depletes the aesthetic quality of water and severely affects aquatic flora and fauna [5]. Some dyes have been classified as carcinogenic, toxic and may cause mutations [6,7]. It is pertinent to employ treatment strategies targeted towards environmental sustainability.

Some treatment methods currently being applied include; physical methods (reverse osmosis, membrane filtration, coagulation), chemical methods (oxidation ion exchange, reduction), and biological methods (aerobic, anaerobic) [8]. Although successful in some cases, the physical and chemical methods lead to problems associated with sludge generation and disposal, and high electricity and operations costs [2]. The biological treatment process is time-consuming and further complicated by toxic and persistent pollutants resistant to degradation, resulting in unpleasant odours [9].

Over the past few decades, advanced oxidation processes (AOPs) have emerged as promising alternatives to conventional methods for destroying organic pollutants [10,11]. These AOPs have exhibited significant advancements, leading to enhanced efficiency in the degradation of various organic pollutants. A key characteristic of advanced oxidation processes (AOPs) is the production of highly reactive hydroxyl radicals, which possess superior oxidative power compared to ozone and hydrogen peroxide. This feature has facilitated the accelerated degradation of organic pollutants [12,13]. Consequently, AOPs have gained prominence and have become preferred alternatives over traditional water treatment methods, due to their remarkable success in effectively degrading organic pollutants [14]. Among the various AOP methods, photocatalysis and its various adaptations have emerged as the most promising technique for industrial applications [13]. Semiconductor oxides, particularly ZnO and its nanocomposites, have been extensively investigated and widely employed as catalysts in photocatalysis.

Due to several key attributes, ZnO has garnered significant attention as a promising material for photocatalysis. These include its non-toxic nature, broad band structure, spectral overlap with solar emission (around 5%), high catalytic activity, cost effectiveness, low toxicity, biological and chemical stability, and ease of application in ambient and harsh environmental conditions [15]. However, problems such as charge carrier recombination, narrow response range to the ultraviolet–visible spectrum, inadequate utilisation efficiency of visible light, susceptibility to dissolution in acidic pH environments, and degradation due to photo-corrosion during extended illumination in aqueous solutions restrict its extensive application. To address these challenges, researchers have explored the modification of ZnO by doping it with additional elements or coupling it with other semiconductors [16]. Modification of ZnO has been reported to mitigate interfacial charge recombination, enhance the presence of surface oxygen vacancies, narrow the bandgap, improve structural stability, and enhance charge carrier separation kinetics [11,17–19]. Additionally, they contribute to enhanced light absorption efficiency beyond the ultraviolet (UV) range, thanks to the phenomenon of localized surface plasmon resonance.

Tungsten trioxide (WO_3), selected as the semiconductor for etching into ZnO, stands out as an *n*-type semiconductor due to its favourable physical and chemical properties. Its notable attributes include a relatively small bandgap (ranging from 2.4 to 2.8eV), in contrast to ZnO's wider bandgap (ranging from 3.2 to 3.37eV). This specific feature empowers WO_3 to capture visible light effectively, positioning it as a prime contender for practical photocatalysis applications. In addition, given the classification of BiOI as a *p*-type semiconductor and its capacity to absorb visible light, BiOI demonstrates a fitting compatibility to establish a *p-n* heterojunction with ZnO, which exhibits absorption capabilities within the ultraviolet (UV) range. Combining BiOI and ZnO can harness a synergistic effect, thereby presenting a potent avenue for enhancing photocatalytic performance.

In this study, we propose the development of an inexpensive, rapid, and straightforward approach for the degradation of methyl orange (MO) in water. This will be achieved through the configuration/design of photocatalysts that combine ZnO with either WO_3 or BiOI. This project aims to address the recombination issues commonly observed in ZnO and enhance its efficiency by employing a strategy of etching with two low band gap semiconductors. Due to their low band gaps, the ternary and transition metal oxides (BiOI and WO_3, respectively) were chosen for this study. These low band gaps enable more efficient utilisation of a broader range of the solar spectrum. Furthermore, the conduction and valence band orientations of BiOI and WO_3 differ from that of ZnO, which is crucial for achieving more effective separation of photoinduced electron-hole pairs, and promoting efficient photodegradation processes. The efficiency of the most efficient heterostructure in this study has been compared to that of other prepared heterostructures in the destruction of MO, from literature. The findings from this research suggest that these novel synthesized heterojunctions can be helpful for dye wastewater elimination and, thus, of importance to the textile industry.

2. Materials and methods

2.1. Chemicals and materials

The starting materials for the synthesis of ZnO–BiOI and ZnO-WO_3 heterostructures include; Potassium iodide (KI), bismuth nitrate pentahydrate ($Bi(NO_3)_3{\cdot}5H_2O$), ammonium metatungstate ($(NH_4)6H_2W_{12}O_{40}$)), and oxalic acid. They were obtained from Sigma-Aldrich. The ZnO precursor, zinc acetate dihydrate ($Zn(CH_3COO)_2{\cdot}2H_2O$) and ethanol were acquired from Associated Chemical Enterprises (ACE). The School of Chemistry at the University of the Witwatersrand supplied the methyl orange dye for this project. A Millipore system was used as a source of purified deionized water during sample preparation. As all the solvents and chemicals used in this project were of the analytical reagent grade, they were used as supplied without additional purification.

2.2. Preparation of heterojunction photocatalysts

Prior to the fabrication of the heterostructures, ZnO was initially synthesized with zinc acetate dihydrate via the sol-gel method. A mixture of ZAD-water was emptied into a reactor on a reflux apparatus set up placed in a water bath. The mixture was allowed to reflux for 30 min at 60 °C under continuous stirring. The gradual introduction of oxalic acid (previously dissolved in alcohol) into the solution resulted in the formation of gels. The reflux was then continued for 60 min at 50 °C. Once the refluxing was complete, the xerogel was cooled to ambient temperature and oven-dried overnight at 80 °C. After drying, the sample was collected and calcined at 500 °C in a furnace to obtain ZnO nanoparticles.

The ZnO-WO_3 based heterojunctions were produced by dispersing pristine ZnO in purified water and continuously stirring for 30 min. Ammonium hydroxide was utilised to maintain a pH of 6.5 in the mixture. The WO_3 starting material $[NH_4)6H_2W_{12}O_{40}]$ was added to the pristine ZnO-water mixture as stirring continued for another 15 h. The precipitate obtained after the reaction was filtered and washed many times with water and then alcohol. The product allowed to dry was subsequently ground and left to air-dry. The ZnO-WO_3 based heterojunction was obtained after calcination at 500 °C for 3 h.

The ZnO–BiOI based heterojunctions were fabricated by suspending pristine ZnO in water before adding $Bi(NO_3)_3.5H_2O$, which had been previously dissolved in alcohol. The resulting mixture of ZnO–$Bi(NO_3)_3.5H_2O$ was stirred continuously as KI, previously dissolved in deionized water was gradually introduced into the mixed liquor. The stirring which continued for another 3 h, was stopped, and the suspension was subsequently centrifuged and allowed to dry in air for 18 h. After collecting the dried product, they were ground, resulting in ZnO-[X]BiOI heterojunction.

2.3. Heterostructures characterization and analytic methods

Surface morphologies and elemental analysis of the prepared composites were determined using a Carl Zeiss Sigma FE-SEM and Oxford X-act EDS. Optical studies and photodestruction evaluation were conducted using a UV 1800 Shimadzu UV–Vis Spectrophotometer, while X-ray diffraction measurements were performed using the Bruker D2 XRD instrument. Textural properties were determined using the Micrometrics TriStar 3000 instrument. The Debye-Scherrer relation was applied to calculate the mean crystallite sizes of the composites from the diffraction peaks, while the band gap was calculated via Tauc's plots derived via the UV–Vis spectra. During the preparation of the heterojunctions, the separation of suspended particles in liquids was achieved with a Hettich ROTOFIX Benchtop Centrifuge. An AM 1.5G 100 mW/cm^2 light source was utilised for this study.

2.4. Photocatalytic performance measurements

The photocatalytic performance evaluation of the heterostructure photocatalysts was assessed in the photodestruction of methyl orange (MO) under simulated solar radiation. In a typical experiment, 50 ml of 10 ppm methyl orange in deionized water was prepared and placed in a 150 ml beaker on a stirrer plate directly under the light source, and the initial concentration was noted. After allowing the pollutant and photocatalyst (20 mg) to equilibrate for 30 min in the dark, the suspensions were magnetically stirred to ensure proper dispersion of the photocatalysts, and the pH was adjusted using HCl and NH_4OH. The photocatalytic activities of each catalyst were then evaluated using an AM 1.5G 100 mW/cm^2 solar radiation simulator, with the suspensions being stirred throughout the experiments. At predetermined intervals, a syringe was used to extract samples from the mixture, which were then filtered using a 0.22 μm membrane filter to remove photocatalyst particles. The filtered samples were analysed using a Shimadzu 1800 spectrophotometer to assess their destruction efficiencies.

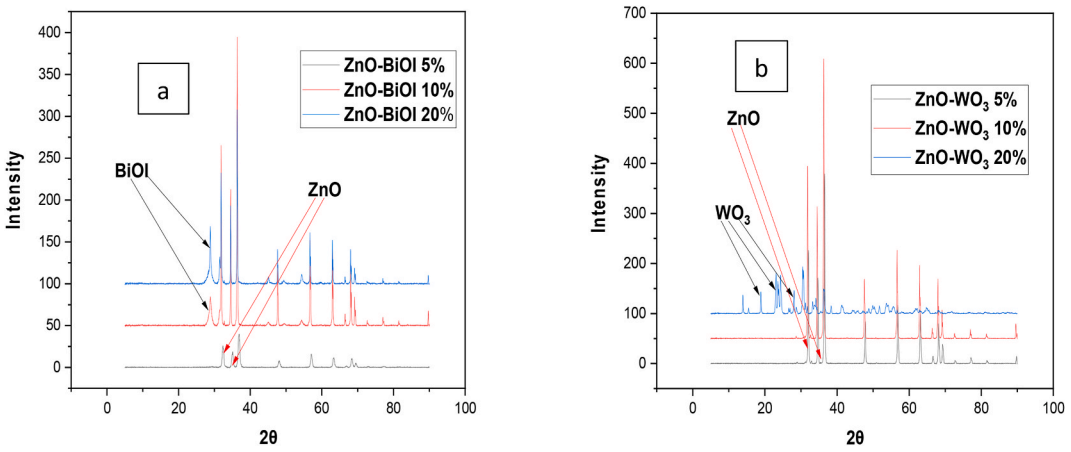

Fig. 1. X-ray diffraction spectra of (a) ZnO–BiOI (X) based heterostructures (b) ZnO-WO_3 (X) based heterostructures.

3. Results and discussion

3.1. Heterostructures characterization

Fig. 1a displays the X-ray diffraction spectra for the 3 ZnO–BiOI based heterojunctions. The heterostructure with 5 % wt. BiOI did not show any peaks of BiOI. This has been ascribed to instrument detection limit and small BiOI doping on the surface of ZnO. The peaks of BiOI can be identified within the ZnO lattice at 10% and 20% doping. The BiOI peak can be identified at 29° and corresponds to the 102-diffraction plane. This peak became more intense at an enhanced doping of 20%, thus, indicating the enhanced doping of BiOI and absolute dispersal in the ZnO lattice. The diffractogram observed from the materials displayed distinct peaks corresponding to the crystalline phases of both BiOI and ZnO in their pure forms. No impurity peaks were detected, thus stipulating an excellent preparation method and sample purity.

The diffraction spectra of the 3 ZnO-WO_3 based heterojunctions are shown in Fig. 1b. The analysed samples exhibited characteristic peaks representative of the triclinic phase of WO_3 and the hexagonal wurtzite structure of ZnO. For the composites containing 5 and 10% WO_3 doping, no supplementary peaks were detected besides those corresponding to the ZnO crystalline structure. The absence of additional peaks can be ascribed to the instrument's limit of detection and effective dispersion of WO_3 on the ZnO surface. The 20% WO_3 doped sample displayed strong peaks observed at 23.0°, 24.4°, 28.0°, and 34.0°, corresponding to the crystal planes 001, 110, 200, and 201 of triclinic WO_3, respectively. These peaks, along with the distinctive peaks of hexagonal ZnO, indicate the complete integration of WO_3 within the lattice of ZnO and sample homogeneity.

The Debye-Scherer relation shown in Equation (1) was applied to determine the mean crystallite sizes of the prepared semiconductor heterojunctions:

$$\boldsymbol{D} = \boldsymbol{K}[(\lambda / (\beta \cos \Theta)] \quad (1)$$

The X-ray diffraction (XRD) measurements were conducted using a wavelength of 1.54056 nm (λ), with θ representing the Bragg

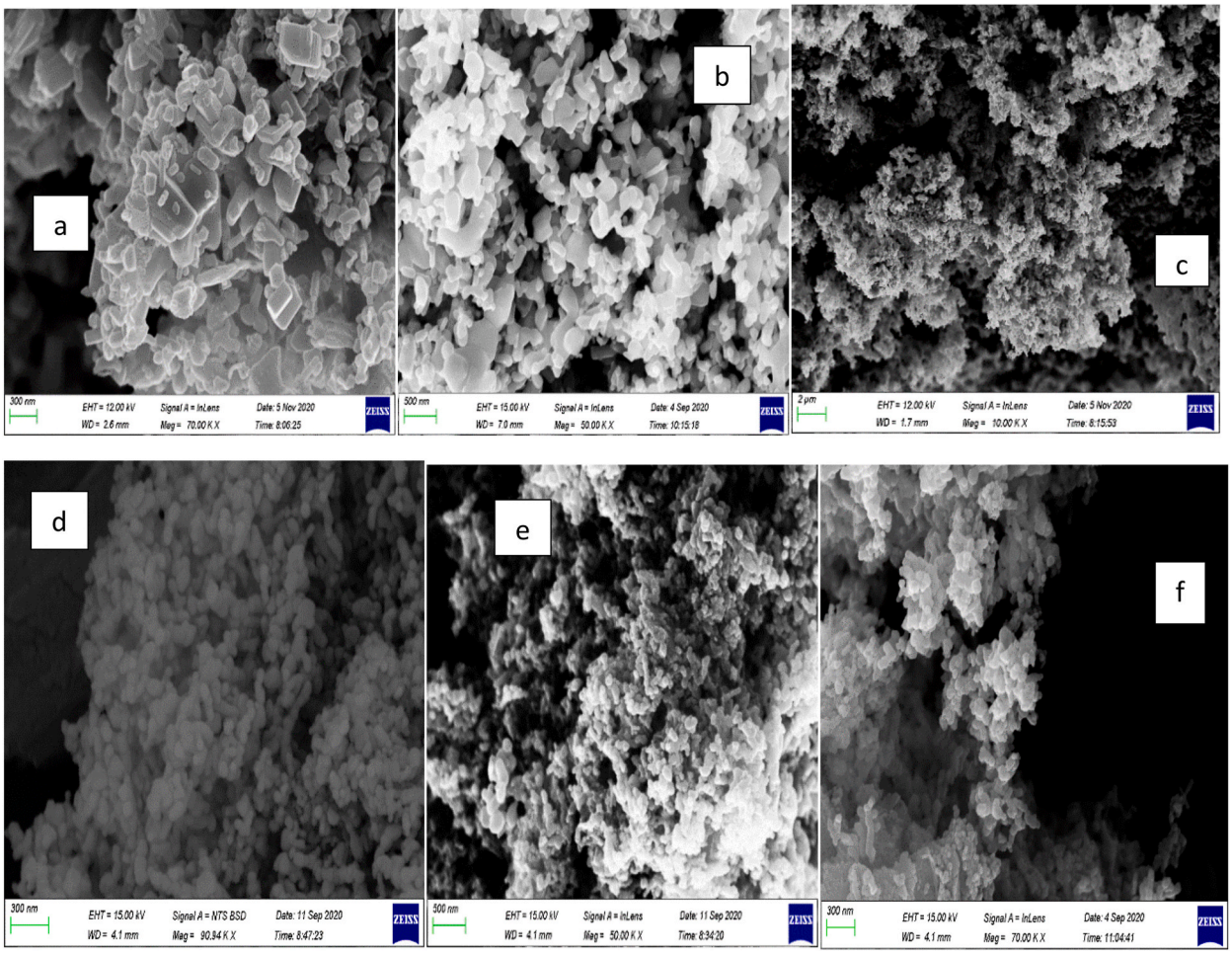

Fig. 2. SEM images of (a) ZnO-[5%]BiOI (b) ZnO-[10%]BiOI (c) ZnO-[20%]BiOI (d) ZnO-[5%]WO_3 (e) ZnO-[10%]WO_3 (f) ZnO-[20%]WO_3.

diffraction angle of the XRD peak and β indicating the measured broadening of the diffraction line peak at an angle 2θ, measured in radians, and corresponding to half of its maximum intensity.

Among the tested samples, the composite with a 5% loading of BiOI exhibited the smallest mean crystallite size, measuring 16.4 nm. In contrast, the samples with 10% and 20% BiOI loadings had larger average crystallite sizes of 31 nm and 45 nm, respectively. As the BiOI loading in the ZnO composite increased, the average crystallite size showed a corresponding increase. This suggests the possibility of the tetragonal BiOI penetrating the hexagonal wurtzite crystal structure of ZnO, which could influence the collapse of crystal growth. The tetragonal BiOI within the ZnO material accounts for the smaller crystallite size observed in the ZnO-[5%]BiOI sample compared to the other samples. Conversely, the enhanced crystallite sizes observed in the other materials can be attributed to the interaction between the two materials. The composite containing 5% wt. loading of WO_3 exhibited a mean crystallite size of 35.4 nm, whereas the sample with 10% WO_3 wt. doping exhibited a mean crystallite size of 49 nm. In the case of the sample with 20% wt. doping of WO_3, the evaluated mean crystallite size was 31 nm.

An FE-SEM was used to investigate the morphologies of heterostructures (Fig. 2a–f). The SEM images revealed non-uniform surfaces of the ZnO–BiOI based composites (5%, 10%, 20%). As the loading of BiOI increased, penetration of rods and rectangular plates was observed, particularly at 10% doping (Fig. 2b), which unveiled the existence of amorphous agglomerates with irregular shapes and the identification of plate-like structures. The sample containing 20% BiOI doping (Fig. 2c) demonstrated a higher degree of agglomeration, leading to a sponge-like morphology characterized by the presence of pores. This agglomeration is likely a result of increased interconnection and wrapping between ZnO and BiOI aggregates. Thus, the morphology was found to depend significantly on the BiOI loading. The SEM images revealed that the WO_3 loadings on the ZnO nanoparticles resulted in agglomeration, displaying a lack of specific and consistent morphological patterns (Fig. 2d–f). Mostly nodular morphology was observed for all three samples, and as the WO_3 loading increased, more clustering was detected. The observed phenomenon can be ascribed to the synthesis technique and initial materials, potentially leading to densely packed clusters of small grains with interconnections. Notably, the sample with a 20% weight loading of WO_3 displayed the most pronounced level of clustering. Supplementary Information 1a-f presents the energy dispersive X-ray spectra of the composites, demonstrating the occurrence of solely the reference elements alongside the expected stoichiometric ratios.

The absorption properties of the composites were analysed with a UV–vis spectrophotometer. The spectra were captured at room temperature within the 200–900 nm wavelength range. To measure the bandgaps of the composites, Tauc's plots were applied along with the Kubelka-Munk relation (Equation (2)). The linear section of the plot depicting $(\alpha h\nu)^2$ versus photon energy was extrapolated to determine the bandgaps, demonstrated in the equation below:

$$\alpha h\nu = A\left(h\nu - E_g\right)^n \tag{2}$$

By extrapolating the linear region on a plot of $(\alpha h\nu)^2$ against $h\nu$, the band gap values can be determined. In this equation, α represents the absorption coefficient, A is a constant, h is Planck's constant, ν denotes the photon frequency, Eg denotes the band gap energy, and n takes the value of 1/2 or 2 depending on whether the transition is direct or indirect, respectively.

Supplementary Information 2 a-f displays the composites' absorption spectra and Tauc's plots. The absorbance measurements of ZnO-[5%]BiOI, ZnO-[10%]BiOI, ZnO-[20%]BiOI, ZnO-[5%]WO_3, ZnO-[10%]WO_3, and ZnO-[20%]WO_3 were recorded at wavelengths of 376 nm, 378 nm, 380 nm, 376 nm, 377 nm, and 380 nm, respectively. The BiOI absorption tail was detected beyond 600 nm, similar to the findings of Qu et al. (2020) [20]. All heterostructures showed a slight red shift, and the ZnO-(X)BiOI heterostructures displayed a band gap narrowing trend with an increase in BiOI loading relative to the pristine ZnO band gap (3.37 eV). The band gap narrowed from 3.37 eV to 3.08 eV with the introduction of BiOI at 5% loading and further to 3.0 eV at 10% loading. Among the different BiOI loadings, the sample with the highest loading of 20% demonstrated the most prominent narrowing of the band gap,

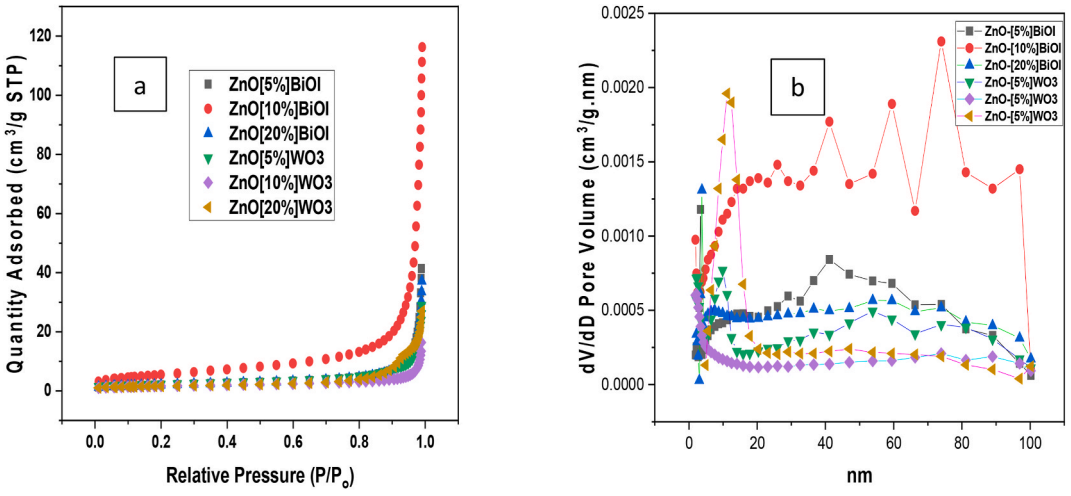

Fig. 3. (a) Nitrogen adsorption-desorption isotherms of the heterostructures (b) Barret-Joyner-Halender (BJH) pore size distribution.

estimated to be 2.20 eV. A corresponding red shift in the absorption spectra of the materials accompanied this narrowing. In the ZnO-[5%]WO_3 heterojunction, a reduction of the band gap was detected compared to the established band gap of pristine ZnO. The estimated band gap for this composite was 2.56 eV. However, with a 10% WO_3 wt. doping, the band gap increased to 3.16 eV. The observed increase in the band gap of the ZnO-[10%]WO_3 composite, which can be ascribed to the emergence of energy level defects within the forbidden band, explains the additional band gap reduction seen in the ZnO-[20%]WO_3 composite. The ZnO-[20%]WO_3 composite exhibited the smallest band gap among the samples, with a value of 2.17 eV. The study by Adhikari et al. (2015) also reported similar findings [21].

The surface area of the synthesized photocatalysts was determined by analysing the nitrogen adsorption-desorption isotherm and obtaining the Barret-Joyner-Halender (BJH) pore distribution curves. The results were then compared with the classification standards provided by the International Union of Pure and Applied Chemistry (IUPAC).

The specific surface areas of the different composites were measured as follows: ZnO-[5%]BiOI - 7.31 m^2/g, ZnO-[10%]BiOI - 19.79 m^2/g, ZnO-[20%]BiOI - 7.30 m^2/g, ZnO-[5%]WO_3 - 7.84 m^2/g, ZnO-[10%]WO_3 - 5.69 m^2/g, and ZnO-[20%]WO_3 - 5.57 m^2/g.

The N_2 adsorption-desorption isotherms (Fig. 3a) demonstrated that all the prepared heterojunctions possessed a mesoporous structure, exhibiting Type IV isotherms. Most of the isotherms showed no hysteresis, except for ZnO-[20%]BiOI and ZnO-[20%]WO_3, which displayed Type H_{III} hysteresis. Analysis of the Barret-Joyner-Halender (BJH) pore size distribution curves revealed a combination of mesopores and macropores in the composites. Specifically, ZnO-[5%]BiOI and ZnO-[10%]BiOI exhibited a higher proportion of macropores compared to mesopores in the analysed samples, as depicted in Fig. 3b. The surface area measurements indicated an increase upon the formation of heterojunctions. However, these increases did not exhibit a consistent pattern.

3.2. Photocatalytic investigation

The efficacy of the synthesized heterostructures was assessed through the photodestruction of methyl orange, measuring their

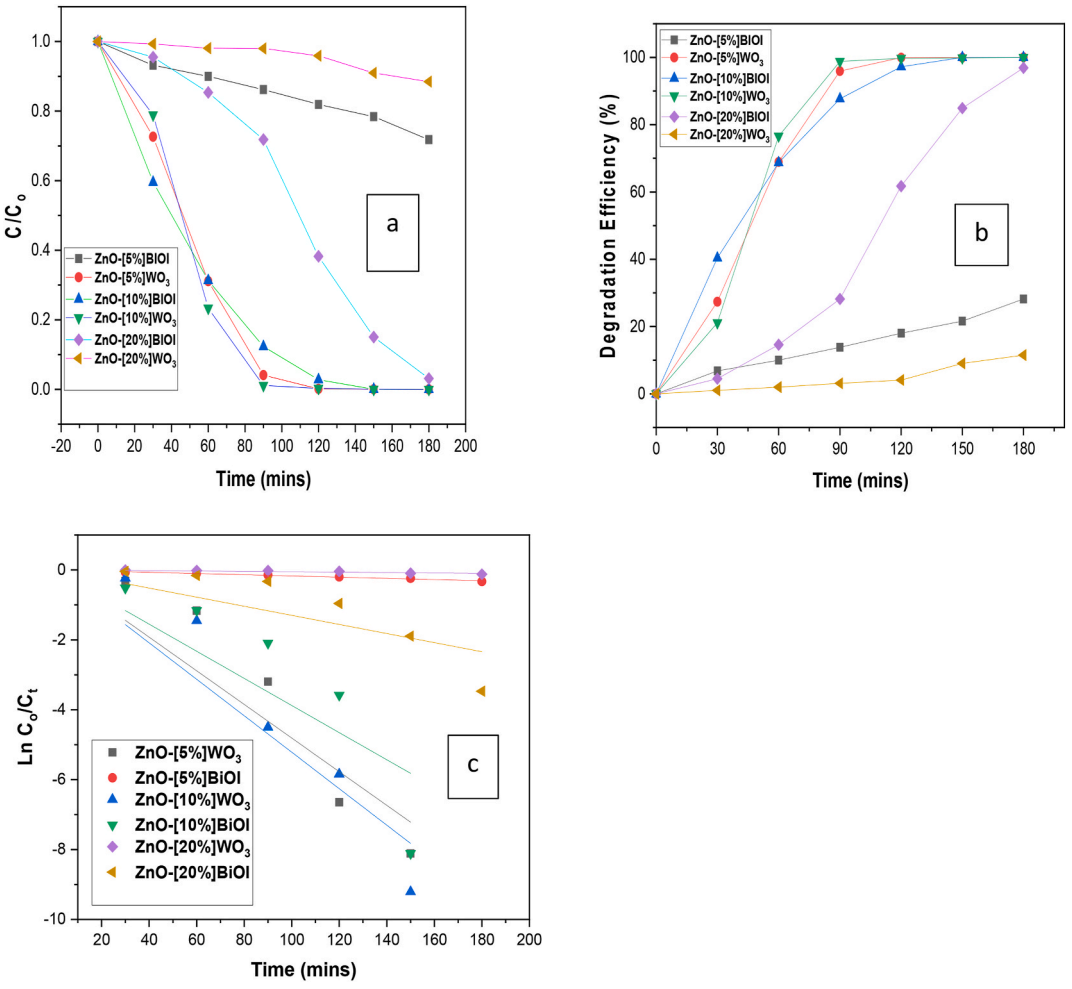

Fig. 4. (a) Photodegradation plot for MO degradation by synthesized heterojunctions (b) Degradation efficiency plot (c) pseudo-first-order kinetic plot of the photodegradation process by heterojunctions.

photocatalytic performance (MO). The destruction plots and efficiencies are displayed in Fig. 4a and b, respectively. It can be deduced that the ZnO-[10%]WO_3 and ZnO-[10%]BiOI samples completely destroyed MO in 90 and 120 min, respectively. The samples with 5 % wt. loading of WO_3 and BiOI into ZnO exhibited varying efficiencies in the photocatalytic removal of MO, as ZnO-[5%]WO_3 destroyed MO in 120 min, while the ZnO-[5%]BiOI heterostructure only achieved approximately 25% removal efficiency even after 180 min of reaction time. A trend change was observed in the ZnO-[20%]WO_3 and ZnO-[20%]BiOI heterostructures, as their MO removal efficiencies were observed at approximately 5% and 100%, respectively, in a total reaction time of 180 min. The poor photocatalytic performance of the ZnO-[20%]WO_3 and ZnO-[5%]BiOI heterostructures are attributed to excessive doping and under doping, respectively. The excess W^{6+} ions affected the light penetration depth into the ZnO structure as it surpassed the space charge region and caused rapid recombination of the charge carriers [22]. It is essential to identify the optimal loading of WO_3 into ZnO for excellent photocatalytic activity, as excess W will create recombination centers which will inhibit photocatalytic performance [23]. A pseudo-first-order kinetic model best expresses the photodegradation kinetics (Fig. 4c). Table 1 presents the apparent first-order reaction kinetics as indicated by the integral linear transform $\ln(C_o/C_t)$ plotted against time. The heterostructures' apparent reaction rate constants (k) and $t_{1/2}$ values are also presented. From the table, it can be observed that it takes approximately 13 min for the MO concentration to be halved to the initial concentration when ZnO-[10%]WO_3 is applied, while it takes approximately 17 min when ZnO-[10%]BiOI is applied. A 10 % wt. optimal doping concentration is adopted in this study, and the two heterostructures (ZnO-[10%]BiOI and ZnO-[10%]WO_3) were additionally utilised to determine the impact of some operational conditions in the photodestruction process.

3.3. Effect of catalyst dose

The amount of photocatalyst used in the reaction can significantly affect the efficiency and cost of the treatment [24]. The influence of catalyst weight was ascertained by varying the masses of the two heterojunction photocatalysts between 2.5 and 40 mg and subsequently applied in the photodestruction process. From the photodestruction plots shown in Fig. 5a–d, it is evident that the destruction efficiency showed a downward trend with the decrease in the dosage of photocatalyst as 67% and 59% destruction efficiencies were observed in 180 min when 2.5 mg of ZnO-[10%]WO_3 and ZnO-[10%]BiOI were applied, respectively. At an increased catalyst dose of 40 mg, a 100% degradation was achieved in 90 min and 120 min when ZnO-[10%]WO_3 and ZnO-[10%]BiOI were applied, respectively. This improved efficiency is ascribed to many reaction sites available to adsorb dye molecules and absorb incident photons from solar radiation. Inappropriate or small quantities of a photocatalyst cause the production of fewer reaction sites on the heterojunction's surface, leading to a reduced photocatalytic performance [25]. The study by Kader et al. (2022) observed a similar outcome.

3.4. Effect of pH

The impact of pH on the photodestruction of MO was ascertained at pH levels of 2, 5, 7, 9 and 11, as shown in Fig. 6a–d. The catalyst weight applied was 20 mg, while the dye concentration was 10 ppm. The results in Fig. 6a–d shows that the best photocatalytic activity for the ZnO-[10%]BiOI heterojunction was observed at pH 7 as MO was eliminated entirely in 120 min. However, excellent photocatalytic activity was also observed at pH 2 and 9 as MO was completely destroyed within a reaction time of 180 min. At pH 5, an 83% degradation efficiency was observed, while the lowest activity of 13% was observed at pH 11. The decline in photocatalytic performance is ascribed to the presence of negative surface charges on the heterojunction. These negative charges reduce the adsorption of MO onto the surface of the ZnO-[10%]BiOI heterostructure. The negatively charged heterojunction intensifies the electrostatic repulsion with the MO anions, further inhibiting their interaction and adsorption on the heterostructure's surface [26].

The optimum performance was observed at pH 7 when ZnO-[10%]WO_3 heterojunction was applied. An excellent photocatalytic performance was also observed at pH 9, as MO was destroyed entirely within a reaction time of 120 min. At pH values of 2, 5 and 11, 47%, 76.5% and 22% degradation efficiencies were observed in 180 min when ZnO-[10%]WO_3 was applied. Generally, the best photocatalytic activities for the destruction of MO were observed at a neutral pH when both heterostructures were applied. The work by Nguyen et al. (2018) and Adeel et al. (2021) observed a similar trend [26,27].

3.5. Effect of MO concentration

To study the effect of methyl orange concentration on the photodestruction process, the initial MO concentration was varied at 5,

Table 1
Photocatalytic degradation of MO and corresponding pseudo-first order reaction kinetic model parameters.

Heterojunction photocatalyst	Destruction efficiency (%)	Time (mins)	R^2	K (min^{-1})	$t_{1/2}$ (min)
ZnO-[5%]WO_3	100	120	0.942	0.0481	14.4
ZnO-[5%]BiOI	25	180	0.996	0.0017	407.7
ZnO-[10%]WO_3	100	90	0.953	0.0521	13.3
ZnO-[10%]BiOI	100	120	0.880	0.0400	17.3
ZnO-[20%]WO_3	5	180	0.909	0.0005	1386.3
ZnO-[20%]BiOI	100	180	0.829	0.013	53.3

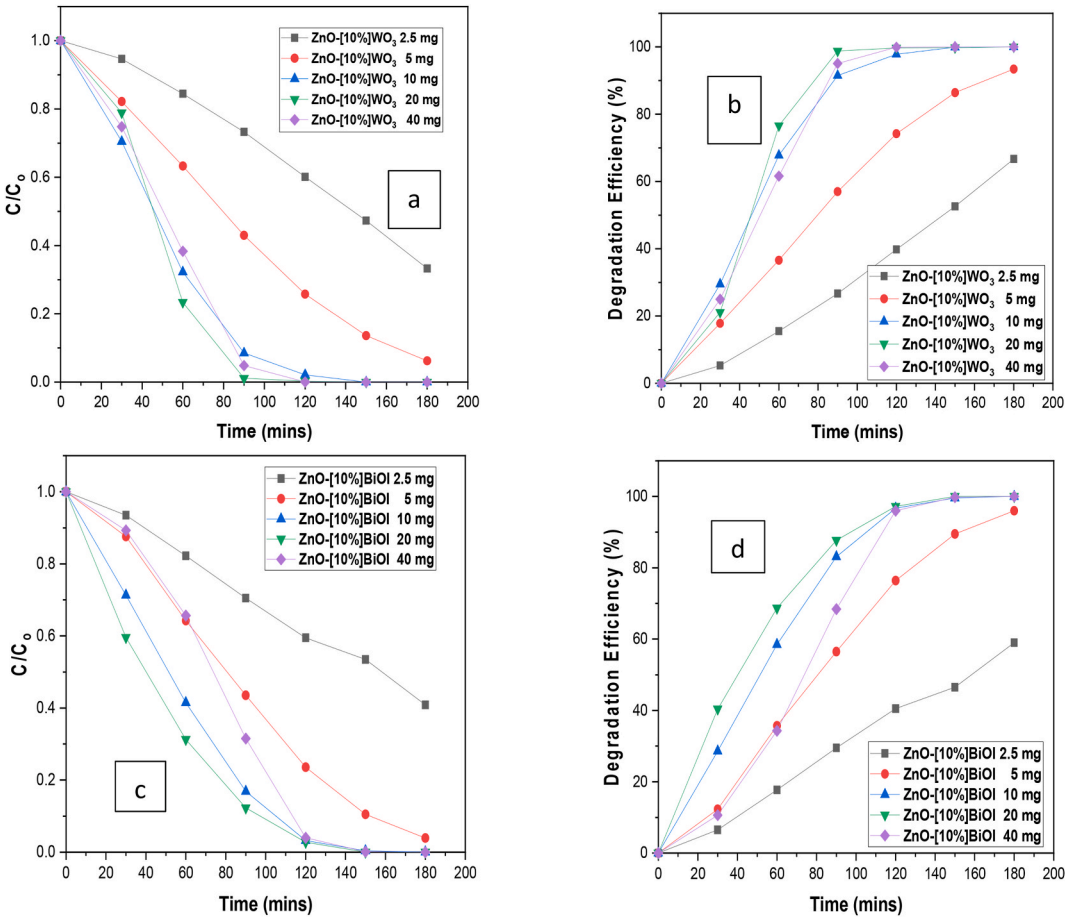

Fig. 5. (a) Photodegradation plot for effect of heterojunction mass using ZnO-[10%]WO_3 (b) Degradation efficiency plot for effect of heterojunction mass using ZnO-[10%]WO_3 (c) Photodegradation plot for effect of heterojunction mass using ZnO-[10%]BiOI (d) Degradation efficiency plot for effect of heterojunction mass using ZnO-[10%]BiOI.

10, 20 and 40 ppm values (Fig. 7a–d). From the destruction plots shown in Fig. 7a, the ZnO-[10%]WO_3 heterojunction destroyed MO at 5, 10 and 20 ppm, corresponding to 60, 90 and 120 min of reaction time, respectively. An inhibited photocatalytic activity was identified at 40 ppm as only approximately 35% degradation efficiency was observed (Fig. 7b). This shows that destruction efficiency decreased with increasing MO concentration. This is ascribed to the depletion of the photogenerated radicals on the heterojunction surface. The reaction centers on the heterojunction's surface, which are responsible for the degradation process, became overwhelmed by the higher concentration of dye molecules [17].

Additionally, the decrease in removal efficiency can be linked to the optical density elevation of the various methyl orange concentrations. As the dye concentration increases, the density of the MO solution also increases. This higher density of the dye solution results in reduced penetration of light into the solution, which, in turn, inhibits the photodegradation efficiency [24]. The ZnO-[10%]BiOI heterojunction was observed to completely eliminate MO at concentration values of 5, 10 and 20 ppm and correspond to reaction times of 120, 120 and 150 min, respectively. At an elevated MO concentration of 40 ppm, an 82% destruction efficiency was observed. Generally, the ZnO-[10%]BiOI heterojunction performed slightly better than the ZnO-[10%]WO_3 heterojunction at most contaminant concentration levels in this study.

3.6. *Suggested photodestruction process*

The photodestruction mechanism of MO by the heterojunction photocatalysts is shown in Fig. 8. During adsorption-desorption equilibration, MO molecules adsorb on the catalyst's surface [28]. When light is incident on the composite material, it generates electron-hole pairs through photoexcitation. The photoexcited electrons are then transferred from the valence band (VB) of BiOI to the conduction band (CB) of ZnO, leaving holes in the VB of BiOI. This electron transfer occurs because the CB of BiOI is more negatively charged (lower energy) compared to the CB of ZnO. Similarly, the VB of ZnO is more positively charged (higher energy) than the VB of BiOI [17]. Repositioning of Fermi levels and the consequent charge migration yield numerous advantageous outcomes. Firstly, the charge migration property of the ZnO–BiOI composite is improved. Separating the charge carriers reduces the likelihood of

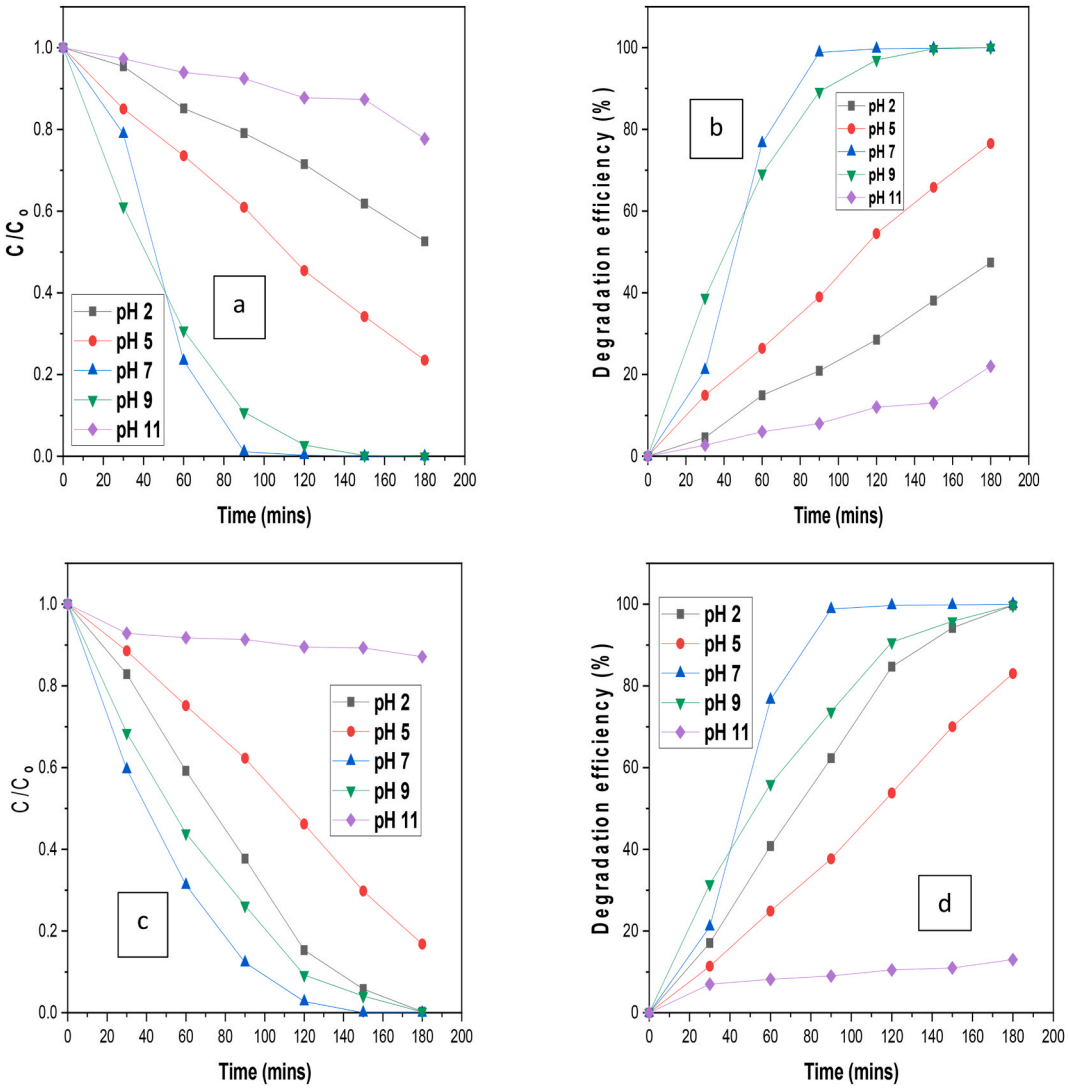

Fig. 6. (a) Photodegradation plot for effect of pH using ZnO-[10%]WO_3 (b) Degradation efficiency plot for effect of pH using ZnO-[10%]WO_3 (c) Photodegradation plot for effect of pH using ZnO-[10%]BiOI (d) Degradation efficiency plot for effect of pH using ZnO-[10%]BiOI.

recombination, where the electron and hole recombine and lose their energy as heat [29]. This leads to a higher efficiency of charge carrier utilisation. Secondly, the improved separation of charge carriers enhances the photo-efficiency of the composite material. Photocatalysis uses light energy to drive chemical reactions, and efficient charge migration is crucial for promoting the desired reactions. With the electrons in the CB of ZnO and the holes in the VB of BiOI, they can engage in separate redox reactions and promote the desired photocatalytic reactions more effectively.

Table 2 shows the photodestruction performance of some photocatalysts and heterojunctions from previously reported studies. It can be deduced that the two heterojunctions prepared in this study have excellent photocatalytic activity and can be applied to treat dye wastewater. The rate constant of the ZnO-[10%]WO_3 is approximately 2-fold higher than that of TiO_2 P25.

4. Conclusion

This study focused on the development, characterization, and subsequent utilisation of various ZnO–WO_3–BiOI based heterojunctions in the treatment of methyl orange (MO). The ZnO-[10%]WO_3 and ZnO-[10%]BiOI were identified as the best performing heterojunctions in this study, as MO was eliminated in 90 and 120 min, respectively. The two best performing heterojunctions were additionally utilised to ascertain the impact of some operational conditions, such as pH, MO concentration, photocatalyst weight. Results obtained show that the degradation efficiency decreased with decreasing photocatalyst dose as 67% and 59% destruction efficiencies were observed in 180 min when 2.5 mg of ZnO-[10%]WO_3 and ZnO-[10%]BiOI were applied, respectively. The optimal performance for the ZnO-[10%]BiOI heterojunction was observed at a pH of 7 as MO was completely eliminated in 120 min. However,

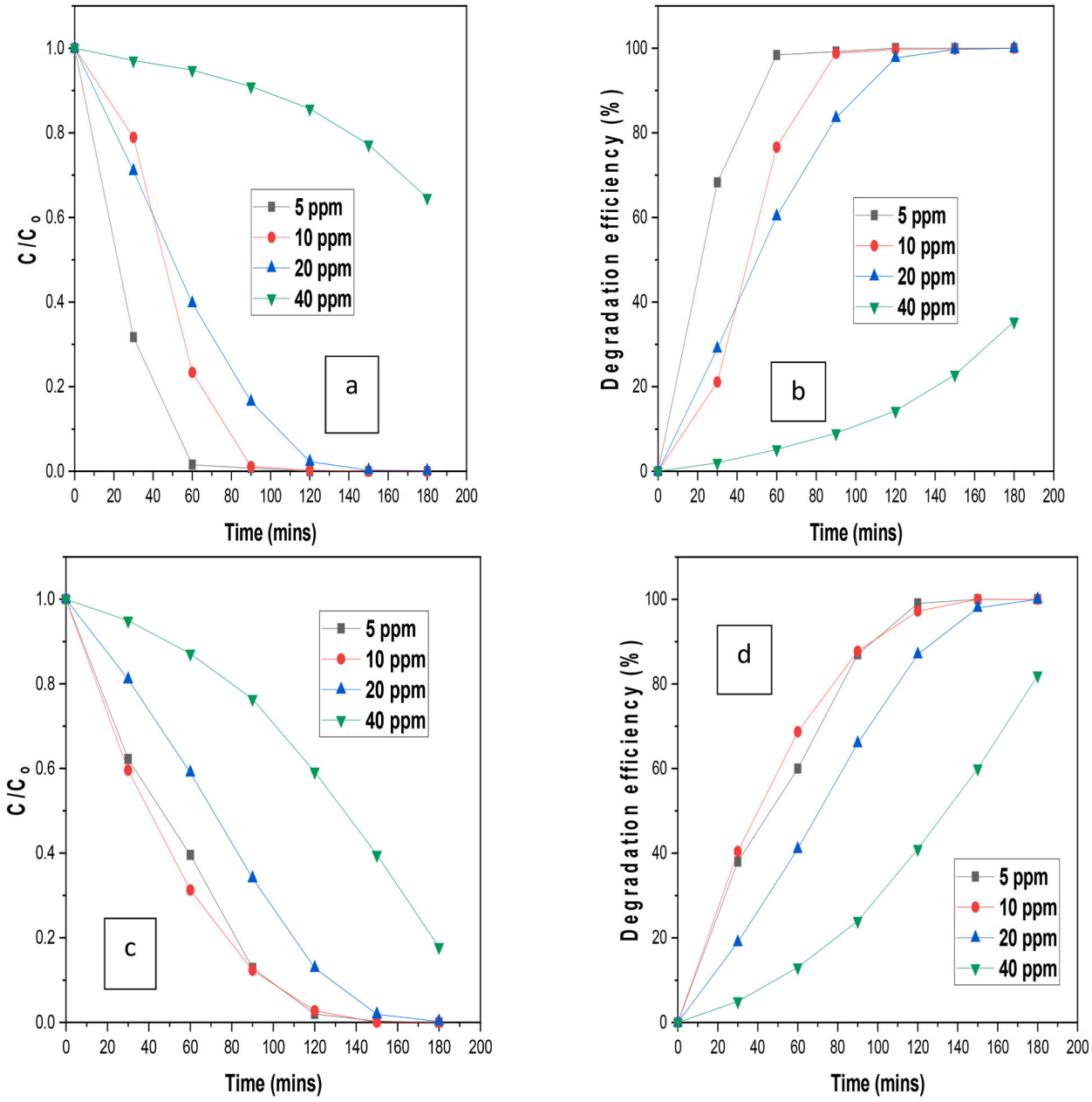

Fig. 7. (a) Photodegradation plot for effect of MO concentration using ZnO-[10%]WO_3 (b) Degradation efficiency plot for effect of MO concentration using ZnO-[10%]WO_3 (c) Photodegradation plot for effect of MO concentration using ZnO-[10%]BiOI (d) Degradation efficiency plot for effect MO concentration using ZnO-[10%]BiOI.

excellent photocatalytic activity was also observed at pH 2 and 9 as MO was completely destroyed within a reaction time of 180 min. At pH values of 2, 5 and 11, degradation efficiencies of 47%, 76.5% and 22% were observed, respectively, in 180 min, when ZnO-[10%]WO_3 was applied. An inhibited photocatalytic activity was identified at 40 ppm as only approximately 35% degradation efficiency was observed. This shows that degradation efficiency decreased with increasing MO concentration. This is ascribed to a depletion in the quantities of photogenerated radicals on the heterostructure surface. A pseudo-first-order kinetic model best expresses the photodegradation kinetics of the photodestruction of MO. It shows that the application of ZnO-[10%]WO_3 leads to a halving of the measured MO concentration to its initial level in approximately 13 min, while it takes approximately 17 min when ZnO-[10%]BiOI was employed.

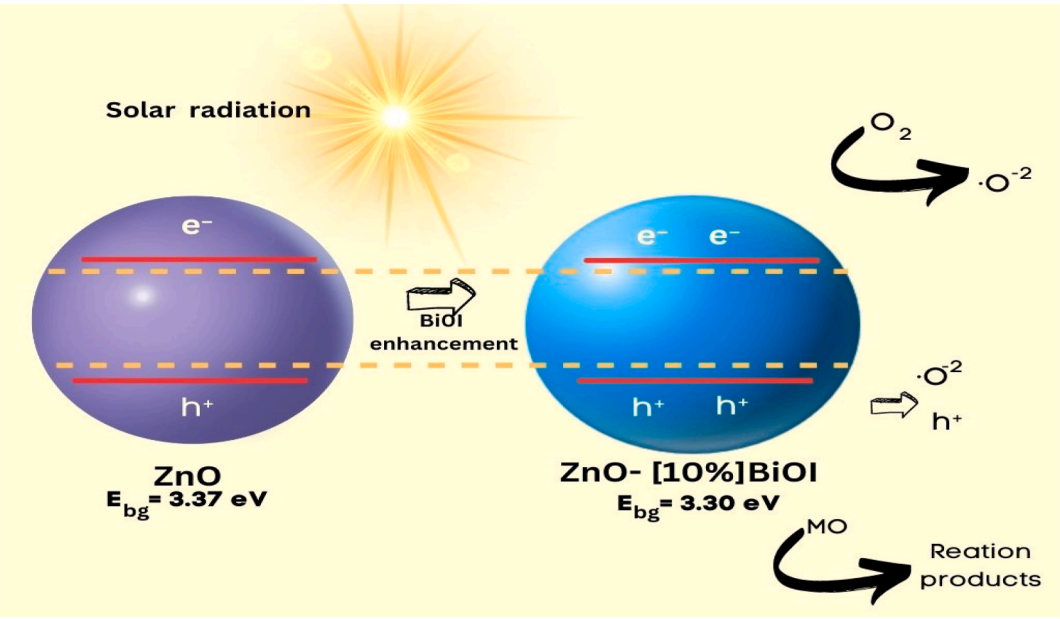

Fig. 8. Influence of BiOI doping and suggested charge transfer process.

Table 2
Photocatalytic performance comparison of various photocatalysts for methyl orange degradation.

Catalyst	MO concentration (ppm)	Removal efficiency (%)	R^2	(k) min^{-1}	Reference
TiO_2-Carbon NPs	20	98	–	0.014	[28]
ZnO/graphene oxide	10	97.7	0.997	0.025	[26]
10% Co–ZnO	100	93	0.95	0.014	[27]
Co:La:TiO_2 nanocomposite	25	98.9	0.998	0.015	[30]
$Ag/MoO_3/TiO_2$	10	75.8	0.981	0.004	[24]
TiO_2 P25	10	75	0.985	0.028	[31]
TiO_2-zeolite + H_2O_2	10	76.9	0.973	0.015	[32]
MoS_2/Co_3O_4 (20%)	20	95.6	–	0.020	[33]
$CuCo_2O_4$	5	85			[3]
ZnO-[10%]WO_3	10	100	0.953	0.052	This study
ZnO-[10%]BiOI	10	100	0.880	0.040	This study

Data availability statement

Has data associated with your study been deposited into a publicly available repository? No.
Data will be made available on request.

CRediT authorship contribution statement

Darlington C. Ashiegbu: Conceptualization, Data curation, Formal analysis, Investigation, Methodology, Validation, Visualization, Writing – original draft, Writing – review & editing. **Herman J. Potgieter:** Conceptualization, Project administration, Resources, Supervision, Visualization, Writing – review & editing.

Declaration of competing interest

The authors declare that they have no known competing financial interests or personal relationships that could have appeared to influence the work reported in this paper.

Appendix A. Supplementary data

Supplementary data to this article can be found online at https://doi.org/10.1016/j.heliyon.2023.e20674.

References

[1] A. Desore, S.A. Narula, An overview on corporate response towards sustainability issues in textile industry, Environ. Dev. Sustain. 20 (2018) 1439–1459, https://doi.org/10.1007/s10668-017-9949-1.

[2] B. Lellis, C.Z. Fávaro-Polonio, J.A. Pamphile, J.C. Polonio, Effects of textile dyes on health and the environment and bioremediation potential of living organisms, Biotechnol. Res. Innov. 3 (2019) 275–290, https://doi.org/10.1016/j.biori.2019.09.001.

[3] L. Gnanasekaran, D. Shanmugapriya, V. Sasikala, S. Vadivel, W.H. Chen, M. Arthi, M. Soto-Moscoso, Nanocubic copper cobaltite for methyl orange degradation through photocatalytic process, Chemosphere 312 (2023), 137311, https://doi.org/10.1016/j.chemosphere.2022.137311.

[4] M.P. Ochoa, V. Estrada, P.M. Hoch, Wastewater stabilisation ponds system: global sensitivity analysis on network design, Chem. Eng. Trans. 50 (2016) 187–192, https://doi.org/10.3303/CET1650032.

[5] J. Kaur, S. Singhal, Facile synthesis of ZnO and transition metal doped ZnO nanoparticles for the photocatalytic degradation of Methyl Orange, Ceram. Int. 40 (2014) 7417–7424, https://doi.org/10.1016/j.ceramint.2013.12.088.

[6] G. De Aragão Umbuzeiro, H.S. Freeman, S.H. Warren, D.P. De Oliveira, Y. Terao, T. Watanabe, L.D. Claxton, The contribution of azo dyes to the mutagenic activity of the Cristais River, Chemosphere 60 (2005) 55–64, https://doi.org/10.1016/j.chemosphere.2004.11.100.

[7] F.M.D. Chequer, T.M. Lizier, R. de Felício, M.V.B. Zanoni, H.M. Debonsi, N.P. Lopes, R. Marcos, D.P. de Oliveira, Analyses of the genotoxic and mutagenic potential of the products formed after the biotransformation of the azo dye Disperse Red 1, Toxicol. Vitro 25 (2011) 2054–2063, https://doi.org/10.1016/j.tiv.2011.05.033.

[8] J. Kaur, S. Bansal, S. Singhal, Photocatalytic degradation of methyl orange using ZnO nanopowders synthesized via thermal decomposition of oxalate precursor method, Phys. B 416 (2013) 33–38, https://doi.org/10.1016/j.physb.2013.02.005.

[9] J. García-Montaño, X. Enech, J.A. García-Hortal, F. Torrades, J. Peral, The testing of several biological and chemical coupled treatments for Cibacron Red FN-R azo dye removal, J. Hazard Mater. 154 (2008) 484–490, https://doi.org/10.1016/j.jhazmat.2007.10.050.

[10] M. Yang, Z. Wang, L. Yao, L. Shi, Construction of 2D/2D $Ti_3C_2/Bi_{12}O_{17}Cl_2$: effective charge separation and improved photocatalytic activity, Mater. Res. Bull. 159 (2023), 112110, https://doi.org/10.1016/j.materresbull.2022.112110.

[11] S. Sampath, V. Rohini, K. Chinnasamy, P. Ponnusamy, S. Thangarasau, W.K. Kim, R.M.R. Vasudeva, M. Shkir, F. Maiz, Solvothermal synthesis of magnetically separable Co–ZnO nanowires for visible light driven photocatalytic applications, Phys. B 652 (2023), 414654, https://doi.org/10.1016/j.physb.2023.414654.

[12] B. Sert, Z. Bilici, O. Kasim, D. Nadir, S.R. Tannaz, A. Khataee, Preparation of S-Scheme g-C_3N_4/ZnO heterojunction composite for highly efficient photocatalytic destruction of refractory organic pollutant, Catalysts 13 (2023) 1–14, https://doi.org/10.3390/catal13030485.

[13] P.V. Gayathri, D. Nair, G. Gopinath, D. Pilla, S. Joseph, Solar photocatalysis for the decontamination of water from emerging pharmaceutical pollutant chloroquine using nano ZnO as the catalyst, water, air, Soil Pollut. 234 (2023) 1–16, https://doi.org/10.1007/s11270-023-06148-4.

[14] N. Roy, K. Kannabiran, A. Mukherjee, Integrated adsorption and photocatalytic degradation based removal of ciprofloxacin and sulfamethoxazole antibiotics using Fc @ rGO-ZnO nanocomposite in aqueous systems, Chemosphere 333 (2023), 138912, https://doi.org/10.1016/j.chemosphere.2023.138912.

[15] Z. Mirzaeifard, Z. Shariatinia, M. Jourshabani, S.M. Rezaei Darvishi, ZnO photocatalyst revisited: effective photocatalytic degradation of emerging contaminants using S-doped ZnO nanoparticles under visible light radiation, Ind. Eng. Chem. Res. 59 (2020) 15894–15911, https://doi.org/10.1021/acs.iecr.0c03192.

[16] R. Liu, D. Zuo, C. Tan, Construction of C/ZnO/BiOI photocatalyst for enhanced degradation of carbaryl: characterization, performance and mechanism, J. Alloys Compd. 911 (2022), 165023, https://doi.org/10.1016/j.jallcom.2022.165023.

[17] D.C. Ashiegbu, N. Moloto, H. Potgieter, Improved photocatalytic activity of ZnO-[10%]BiOI and ZnO-[10%]WO_3 heterostructure in the destruction of 2-chlorobiphenyl, Env. Sci. Adv. 2 (2023) 325–338, https://doi.org/10.1039/D2VA00222A.

[18] Y.Y. Wang, A.Q. Gong, W.H. Yu, Synthesis and photocatalytic characterization of ZnO/BiOI microspheres, Chin. J. Inorg. Chem. 33 (2017) 509–518, https://doi.org/10.11862/CJIC.2017.061.

[19] J. Yi, G. Zhang, Y. Wang, W. Qian, X. Wang, Recent advances in phase-engineered photocatalysts : classification and diversified applications, Materials 16 (2023) 1–17, https://doi.org/10.3390/ma16113980.

[20] Z. Qu, Y. Su, L. Sun, F. Liang, G. Zhang, Study of the structure, electronic and optical properties of BiOI/Rutile-TiO2 heterojunction by the first-principle calculation, Materials 13 (2020), https://doi.org/10.3390/ma13020323.

[21] S. Adhikari, D. Sarkar, G. Madras, Highly efficient WO_3-ZnO mixed oxides for photocatalysis, RSC Adv. 5 (2015) 11895–11904, https://doi.org/10.1039/c4ra13210f.

[22] M. Russo, G. Iervolino, V. Vaiano, W-doped zno photocatalyst for the degradation of glyphosate in aqueous solution, Catalysts 11 (2021) 1–18, https://doi.org/10.3390/catal11020234.

[23] S. Anandan, A. Vinu, K.L.P. Sheeja Lovely, N. Gokulakrishnan, P. Srinivasu, T. Mori, V. Murugesan, V. Sivamurugan, K. Ariga, Photocatalytic activity of La-doped ZnO for the degradation of monocrotophos in aqueous suspension, J. Mol. Catal. A: Chem. 266 (2007) 149–157, https://doi.org/10.1016/j.molcata.2006.11.008.

[24] S. Kader, M.R. Al-Mamun, M.B.K. Suhan, S.B. Shuchi, M.S. Islam, Enhanced photodegradation of methyl orange dye under UV irradiation using MoO_3 and Ag doped TiO_2 photocatalysts, Environ. Technol. Innov. 27 (2022), 102476, https://doi.org/10.1016/j.eti.2022.102476.

[25] P. Latha, K. Prakash, S. Karuthapandian, Effective Photodegradation of CR & MO dyes by morphologically controlled Cerium oxide nanocubes under visible light Illumination, Optik 154 (2018) 242–250, https://doi.org/10.1016/j.ijleo.2017.10.054roy.

[26] V.N. Nguyen, D.T. Tran, M.T. Nguyen, T.T.T. Le, M.N. Ha, M.V. Nguyen, T.D. Pham, Enhanced photocatalytic degradation of methyl orange using ZnO/graphene oxide nanocomposites, Res. Chem. Intermed. 44 (2018) 3081–3095, https://doi.org/10.1007/s11164-018-3294-3.

[27] M. Adeel, M. Saeed, I. Khan, M. Muneer, N. Akram, Synthesis and characterization of Co-ZnO and evaluation of its photocatalytic activity for photodegradation of methyl orange, ACS Omega 6 (2021) 1426–1435, https://doi.org/10.1021/acsomega.0c05092.

[28] A.R. Kuldeep, A.S. Bhosale, K.M. Garadkar, Enhanced photocatalytic performance of TiO_2–carbon nanocomposite, J. Mater. Sci. Mater. Electron. 31 (2020) 9006–9017, https://doi.org/10.1007/s10854-020-03434-3.

[29] B. Parasuraman, B. Kandasamy, I. Murugan, M.S. Alsalhi, N. Asemi, P. Thangavelu, S. Perumal, Designing the heterostructured $FeWO_4/FeS_2$ nanocomposites for an enhanced photocatalytic organic dye degradation, Chemosphere 334 (2023) 1–9, https://doi.org/10.1016/j.chemosphere.2023.138979.

[30] K. Azad, P. Gajanan, Photodegradation of methyl orange in aqueous solution by the visible light active Co:La:TiO2 nanocomposite, Chem. Sci. J. 8 (2017) 1–9, https://doi.org/10.4172/2150-3494.1000164.

[31] B. Regraguy, M. Rahmani, J. Mabrouki, F. Drhimer, I. Ellouzi, C. Mahmou, A. Dahchour, M. El Mrabet, S.El Hajjaji, Photocatalytic degradation of methyl orange in the presence of nanoparticles $NiSO_4/TiO_2$, Nanotechnol. Environ. Eng. 7 (2022) 157–171, https://doi.org/10.1007/s41204-021-00206-0.

[32] A.P. Aziztyana, S. Wardhani, Y.P. Prananto, D. Purwonugroho, Darjito, Optimisation of methyl orange photodegradation using TiO2-zeolite photocatalyst and H_2O_2 in acid condition, IOP Conf. Ser. Mater. Sci. Eng. 546 (2019), 042047, https://doi.org/10.1088/1757-899X/546/4/042047.

[33] T.M. Tien, C.H. Chen, C.T. Huang, E.L. Chen, Photocatalytic degradation of methyl orange dyes using green synthesized MoS_2/Co_3O_4 nanohybrids, Catalysts 12 (2022), https://doi.org/10.3390/catal12111474.